

# Broadband Ground Motions from Dynamic Models of Rupture on the Northern San Jacinto Fault, and Comparison with Precariously Balanced Rocks

by Julian C. Lozos,\* Kim B. Olsen, James N. Brune, Rumi Takedatsu,  
Richard J. Brune, and David D. Oglesby

**Abstract** The Southern California San Jacinto fault is geometrically complex, consisting of several major strands with smaller scale complexity within each strand. The two northernmost strands, the Claremont and the Casa Loma–Clark, are separated by a 25-km-long extensional stepover with an average of 4 km separation between the strands. We use a combined modeling method to assess probable rupture and ground-motion behaviors for this stepover. First, dynamic rupture modeling on geometrically complex fault strands embedded in a state-of-the-art 3D crustal velocity model is used to generate a series of scenario earthquakes. We then use the resulting near-fault low-frequency (<1 Hz) ground-motion time histories to generate broadband synthetic seismograms with a hybrid approach. These synthetics are then compared with a distribution of precariously balanced rocks (PBRs) near the fault to constrain our results and assess shaking hazard for the region surrounding the fault. Our dynamic models produce sources between  $M_w$  5.4 and 6.9, with rupture limits imposed by sharp contrasts in fault stress or by geometrical barriers. The main stepover serves as a primary barrier to rupture in our model, producing event sizes that are consistent with the historical behavior of the San Jacinto fault. The largest broadband synthetics are a good match to leading ground-motion prediction equations and are generally consistent with the distribution of PBRs, none of which experience accelerations that produce toppling probabilities significantly higher than zero. Thus, although the PBRs do not rule out any of our model scenarios, they confirm that our models produce realistic rupture extents and shaking.

*Online Material:* Figures of total slip for additional rupture models, low-frequency intensity plots, synthetic seismograms, and comparison with ground-motion prediction equations.

## Introduction

The San Jacinto fault (SJF) is a major right-lateral strike-slip component of the San Andreas fault system in inland southern California. The San Jacinto and San Andreas faults jointly accommodate up to 80% of the plate boundary strain in the region (Fialko, 2006; Blisniuk *et al.*, 2010). The entire length of the SJF, from its approach to the San Andreas fault in Cajon Pass near San Bernardino, to its terminus in the Imperial Valley, is ~230 km (Fig. 1). However, its structure is not continuous for that whole length; it consists of several long

strands, separated by stepovers or splays, some of which have considerably smaller-scale geometrical complexity as well.

The instrumental record of ruptures on the SJF includes eight  $M_w$  6+ events since 1890. Only two of these, the 1918  $M_w$  ~ 6.9 event near Hemet (Salisbury *et al.*, 2012) and the 1968  $M_w$  6.5 Borrego Mountain earthquake (Allen *et al.*, 1968) produced measurable surface rupture. Isoseismals for these and other events suggest they were confined to individual strands of the fault (Sanders and Kanamori, 1984; Toppozada *et al.*, 2002). These records suggest that, despite the length of the fault and its high slip rate, some property of the fault is restricting its regular rupture behavior to only moderately large events. Analysis of measured surface rupture traces

\*Now at Department of Geophysics, Stanford University, Mitchell Building 3rd Floor, 397 Panama Mall, Stanford, California 94305; jlozos@stanford.edu.

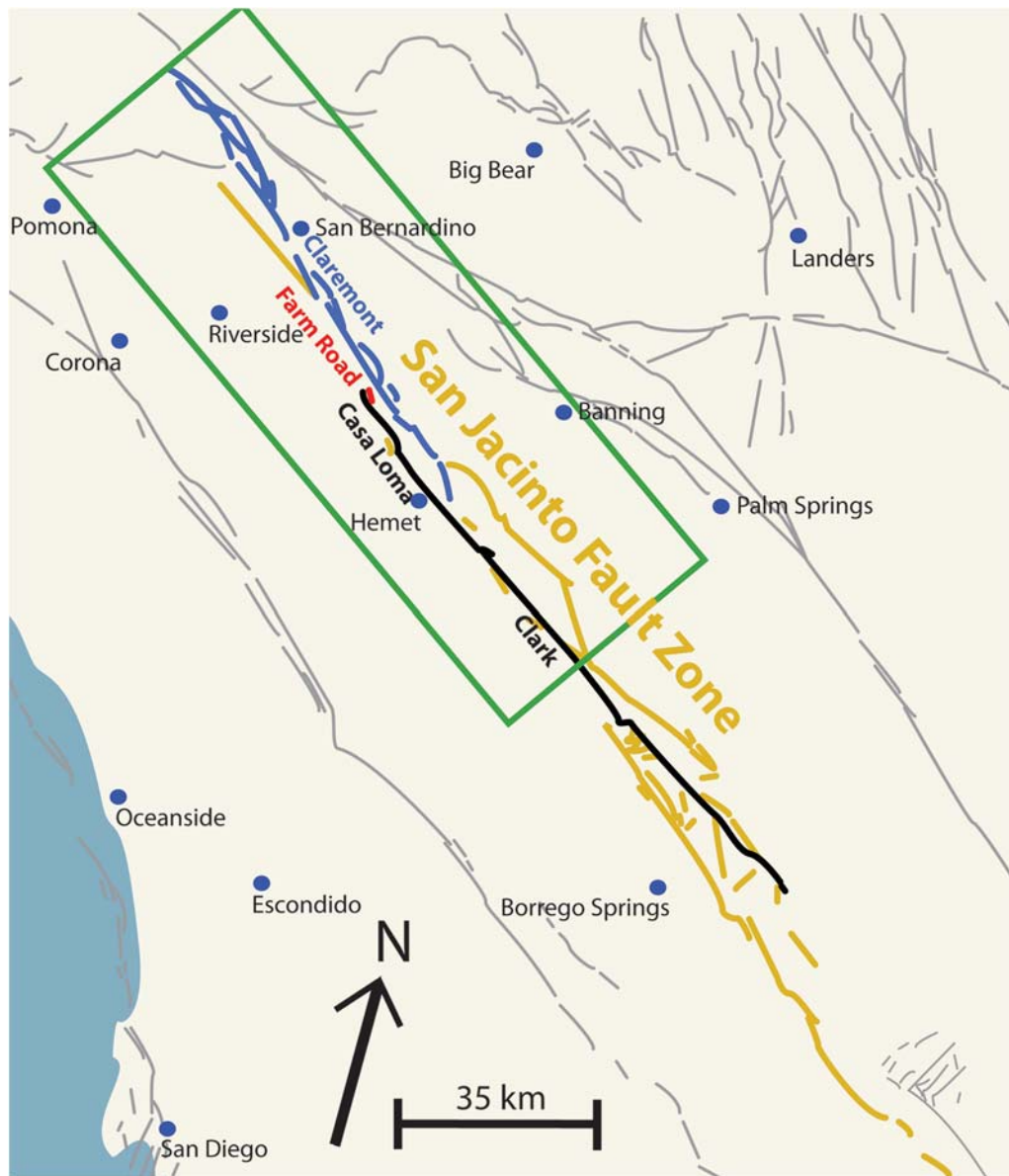


**Figure 1.** Map of the San Jacinto fault (SJF) zone, with a geometry based on the U.S. Geological Survey (USGS) Quaternary faults database (USGS, 2010; see [Data and Resources](#)). The Claremont strand is shown in blue, the Farm Road strand in red, and the Casa Loma–Clark strand in black. Other strands of the SJF are shown in yellow, and other Quaternary faults are shown in gray. The cities are indicated with blue dots. The area of the present study is enclosed in the green box.

(Wesnousky, 2008), as well as dynamic rupture models of fault stepovers (e.g., Harris and Day, 1993; Aochi *et al.*, 2000; Oglesby, 2008; Lozos *et al.*, 2012) and branches (Kame *et al.*, 2003; Duan and Oglesby, 2007) suggest that geometrical complexities often serve as endpoints for ruptures. Given the multistranded geometry of the SJF, this may be one explanation for the size of its historic events.

The northernmost of the major geometrical discontinuities along the SJF trace is the extensional stepover between the Claremont strand, which runs from Cajon Pass to the city of San Jacinto, and the Casa Loma–Clark strand, which runs from Moreno Valley to 20 km east-northeast of Borrego Springs (Fig. 1). The two strands overlap for 25 km along strike. The

separation between the strands through the stepover region ranges from 2.5 to 5 km. A smaller strand of  $\sim 2.5$  km length, the Farm Road, is positioned at the northern end of the overlap, halfway between the Claremont and Casa Loma strands. The primary fault strands bound the San Jacinto Valley, a 2.3-km-deep pull-apart sedimentary basin (Park *et al.*, 1995). Two moderate historic events, an  $M_w \sim 6.5$  in 1899 and an  $M_w \sim 6.9$  in 1918, are known to have occurred in the stepover region, only the latter of which produced surface rupture. The lack of surface rupture means that these historic-type events would not appear in paleoseismic trenches. However, the paleoseismic record for both the Claremont (Onderdonk *et al.*, 2013, 2015) and the Casa Loma–Clark (Rockwell *et al.*,

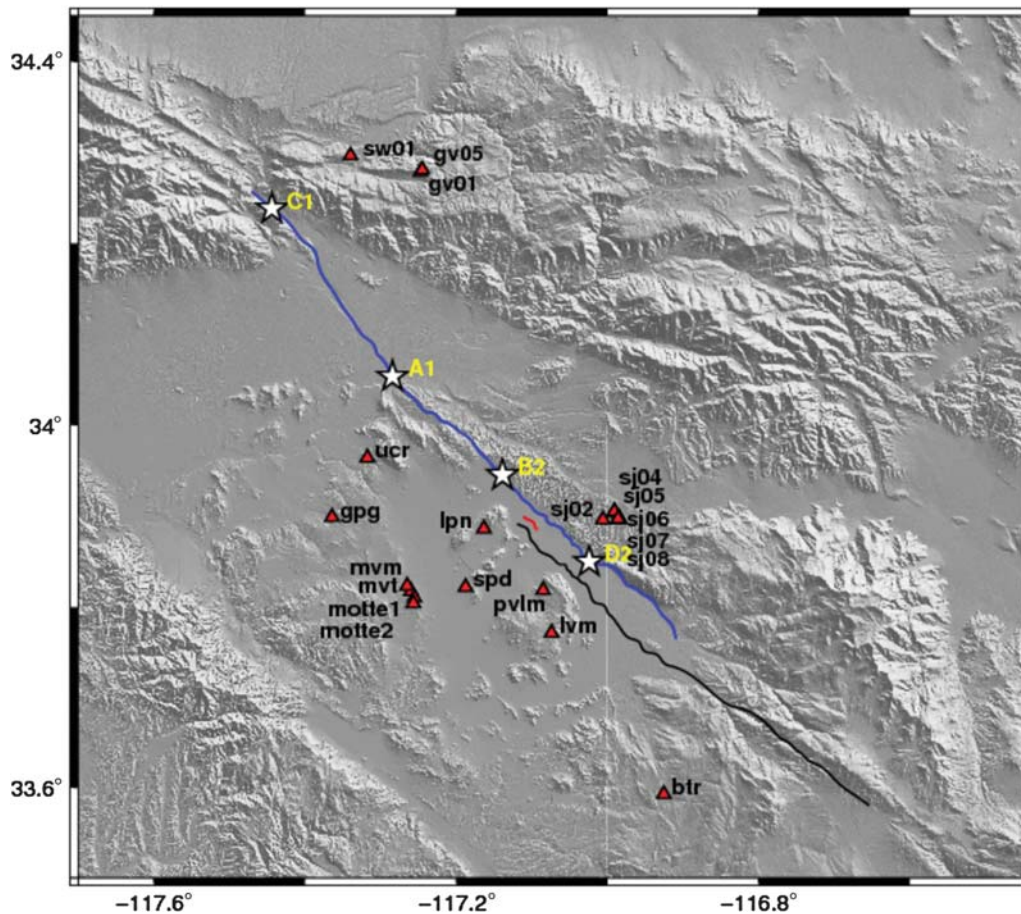


**Figure 2.** Map of the northern SJF, from Cajon Pass (northwest corner of this map) to Anza (southeast corner). The blue trace depicts the Claremont strand, the red trace is the Farm Road strand, and the black trace is the Casa Loma strand. The stars depict the epicenters of the four rupture scenarios for which broadband seismograms were calculated. The triangles mark the 20 precariously balanced rock (PBR) sites described in this study (Table 1).

2015) indicates that significantly larger events, with an average slip per event of 2.5–3 m, have occurred on each strand multiple times in the past, some close enough together in time to have possibly been a single rupture.

This returns to the questions of how fault complexity affects rupture length, what conditions lead to a rupture propagating through complexities that have served as barriers in the past, and whether a single event can rupture across the stepover between the Claremont and Casa Loma–Clark strands of the SJF. The average 4 km separation between the strands is the maximum extensional stepover width that allows jumping rupture in modeling studies of idealized disconnected stepovers (Harris and Day, 1993; Lozos *et al.*, 2012), a result that bears out in analysis of historical rupture traces (Wesnousky, 2008). The presence of more than a dozen precariously balanced rocks (PBRs, see Fig. 2) near the stepover region (Brune, 1996, 2002; Brune *et al.*, 2006), however, indicates that something has prevented the ground acceleration near the faults from reaching the level required to topple the rocks over multiple earthquake cycles. Whether this is an effect of the dynamics of extensional stepovers resulting in lower ground motion (Brune, 2002; Lozos *et al.*, 2013) or an

indication that the stepover is a primary barrier to rupture cannot be determined from historical data alone.

To address these questions, we implement a multitiered modeling approach. We use 3D dynamic rupture modeling to investigate the effects of complex fault geometry, stress conditions, and surrounding geology on rupture propagation and slip. Although this method best describes the physics of the source, it is very computationally intensive; the discretization used in these models is such that only low-frequency (LF) ground motions are well resolved. However, toppling probabilities for PBRs are affected by both LF and high-frequency (HF) ground motions (Purvance *et al.*, 2008). We therefore combine the near-fault LF (< 1 Hz) ground-motion time histories generated by the dynamic models with HF scattering functions (Olsen and Takedatsu, 2014) to produce broadband seismograms for each model rupture, while also accounting for additional complexity in the medium surrounding the faults. We then conduct toppling tests for models of the PBRs in the study area, using these synthetic seismograms. Any models that produce ground motions that would topple many of the rocks can be ruled out as plausible scenarios, but scenarios that produce ground motions that are consistent with

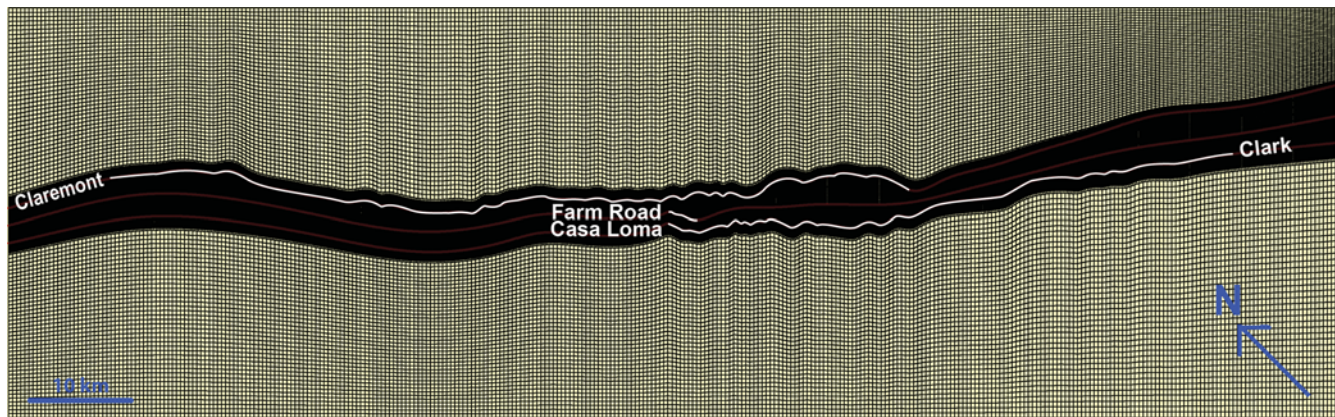


**Figure 3.** Mesh of the SJF, generated with FaultMod (Barall, 2009), as used in our dynamic models. The parts of the fault that are able to rupture are marked in white. The Claremont strand is to the left in this figure, the Casa Loma to the right, and the Farm Road is between them. The grid size is 100 m in the near field, and 400 m in the far field.

the distribution of rocks may also indicate what types of rupture behaviors have happened in the past, as well as what intensity of ground shaking may be expected in the vicinity of the Claremont/Casa Loma–Clark stepover in the future.

## Methods

### Source Models

We model our earthquake sources using FaultMod (Barall, 2009), a 3D finite-element code that has performed well in the Southern California Earthquake Center (SCEC) dynamic rupture code validation exercise (Harris *et al.*, 2009). We incorporate a slip-weakening Coulomb friction criterion (Ida, 1972; Palmer and Rice, 1973; Andrews, 1976) and a fully elastic medium. Our critical slip-weakening distance is 0.4 m, and our dynamic coefficient of friction is 0.2; the static frictional coefficient varies around 0.6, depending on the stress state, as described below. Our mesh is generated within FaultMod, with 100 m elements immediately adjacent to the fault and 400 m elements in the far field. We nucleate rupture at specified locations by raising the shear stress to 10% above the yield stress and forcing the rupture to propagate outward over a 3 km radius.

Our model region covers the northwestern end of the SJF in Cajon Pass southeast to Anza, site of a known seismic gap, for an overall system length of 106.8 km. The fault geometry along strike is based on the U.S. Geological Survey (USGS) Quaternary Faults Database (USGS, 2010; see [Data and Resources](#)); the Claremont strand is 75.6 km long, the Casa Loma–Clark is 55 km, and the Farm Road is 2.4 km. The actual fault geometry down-dip is poorly constrained. Thus, for simplicity, we use a vertical dip for all three strands, as in the SCEC Community Fault Model (Plesch *et al.*, 2007), an interpretation that is consistent with geology (Kendrick and Morton, 2012) and seismicity literature (Lin *et al.*, 2007). Our fault mesh is shown in Figure 3. The fault trace is likely to be smoother at depth than at the surface, but we retain the

surface variation at depth, thus making this model setup an end member for complex fault geometry.

We implement a regional stress field combined with stochastic asperities. Seismicity relocation shows a regional stress orientation of N7°E for the northern SJF (Hardebeck and Hauksson, 2001). We use a N7°E-oriented stress tensor that produces a stress drop of 5.5 MPa and a strength parameter  $S$  of 0.6 (defined as the difference between the yield stress and the initial shear stress, divided by the dynamic stress drop) when resolved onto a planar fault of the average strike of the SJF, as in the lower-resolution models of the Claremont–Casa Loma stepover in the companion article to this study (Lozos *et al.*, 2015). This low  $S$  value would result in supershear rupture velocities on a planar fault in a homogeneous setting, but the complexity of our model prevents the rupture front from exceeding the shear-wave velocity. We then resolve this homogeneous tensor onto our complex fault geometry, which results in a pattern of effective higher and lower stress drops that corresponds with the bends in the fault.

To account for additional stress complexity that may be generated by factors that are not purely geometrical, such as interactions with other nearby faults, we also include stochastically generated shear stress asperities, using the method of Andrews and Barall (2011), which creates a random self-similar shear stress distribution based on fault dimensions, a specified normal stress value, and four random number seeds. We use the average normal stress value from the regional stress field and four sets of random numbers to produce four different stochastic shear stress distributions in which the dimensions of the smallest patch of stress correspond to the length of the smallest bend in the model fault trace. We then combine each resulting set of asperities with the regional stress field by subtracting the average shear stress value for the regional stress field from the shear stress value at each point of the stochastic stress field, then adding the remaining shear stress back to the regional value at that same point. Lastly, we taper the stresses toward the surface to a value of 10% of their

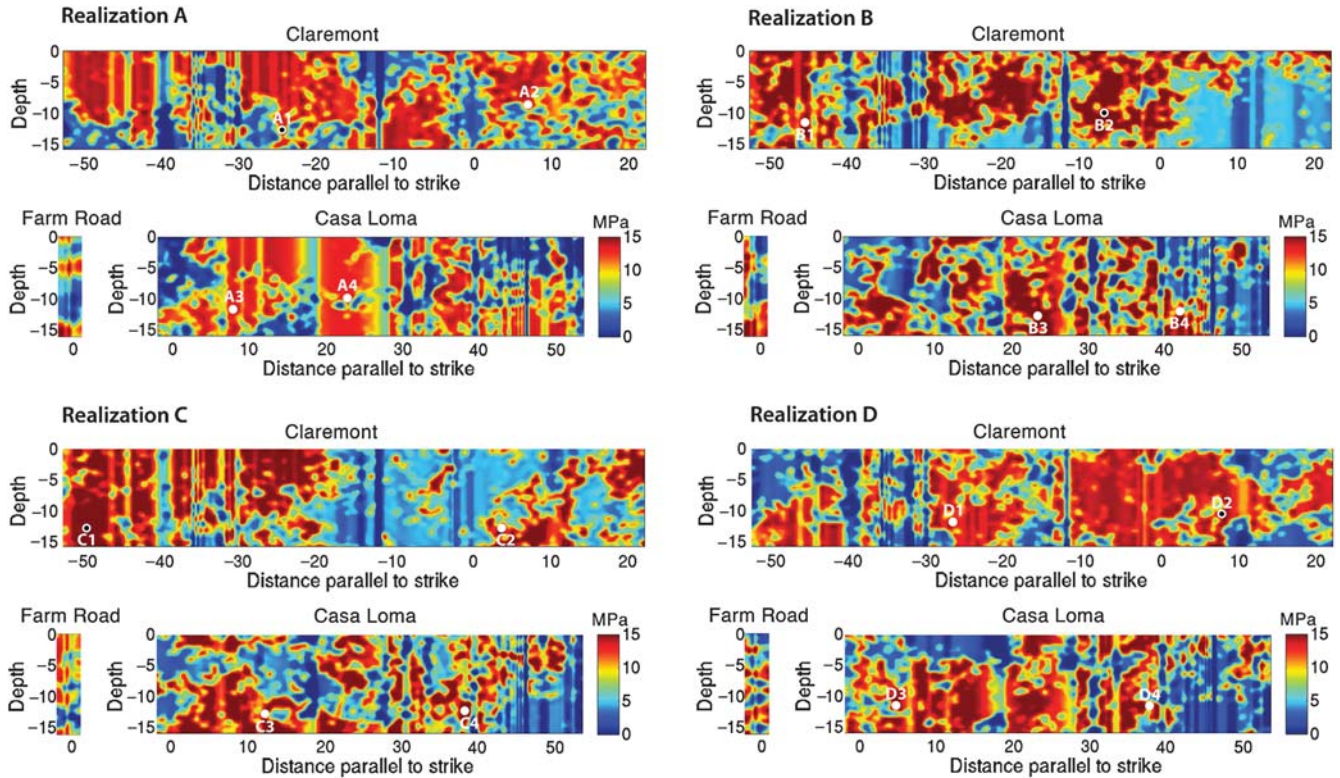


**Figure 4.** Four combined regional and stochastic shear stress realizations. The irregular patches are stochastic asperities, and the vertical banding is contributed by the regional stress field. Note that the normal stress field is purely regional and lacks the asperities shown here. The lettered white dots on each plot are the forced nucleation points for our dynamic models. The dots with the black centers are the nucleation points that produced the largest ruptures; these are the ones we used to produce full broadband synthetic seismograms.

value at depth over the top 3 km of the fault and set the minimum shear stress value to 0 MPa to prevent the fault from slipping left laterally. The resulting shear stress fields, prior to tapering, are shown in Figure 4. The lettered dots are forced nucleation locations, selected because they correspond with large areas of high shear stress.

We assign 3D material properties from the SCEC Community Velocity Model (CVM-S, [Magistrale et al., 2000](#)) to the modeled volume. Contrasts in material properties can affect the dynamics of earthquake rupture ([Andrews and Ben-Zion, 1997](#); [Harris and Day, 1997](#); [Lozos et al., 2013](#)), so we include them even though the dynamic models are not used to determine ground motions at higher frequencies. We nevertheless clip the minimum  $S$ -wave velocity to 1200 m/s, such that the dynamic models still resolve LF ground motions up to an estimated 1 Hz.

#### Broadband Models

To include the HF component of the ground motions at the PBR sites, we use the hybrid broadband generation method BBtoolbox v.1.5 ([Olsen and Takedatsu, 2014](#)). This method combines deterministic LF synthetics computed using kinematic or dynamic descriptions in 1D or 3D media, with HF scatterograms. The HF scatterograms are generated for each component of motion based on the theory for multiple

$S$ -to- $S$  scattering by [Zeng et al. \(1991, 1993\)](#). The scatterograms are based on user-specified site scattering parameters and are partly based on the site-specific velocity structure. The seismic-scattering wave energy is realized to appear after the direct  $P$ -wave arrival time, which is found from 3D ray tracing ([Hole, 1992](#)). Finally, the scatterograms are convolved with an appropriate source time function. It is assumed that the scattering operators and moment release originate throughout the fault but start at the hypocenter. The hybrid broadband seismograms are calculated in the frequency domain using a simultaneous amplitude and phase-matching algorithm ([Mai and Beroza, 2003](#)).

The version of BBtoolbox used here (v.1.5, [Olsen and Takedatsu, 2014](#)) has been revised from previous versions ([Mai et al., 2010](#); [Mena et al., 2010](#)) in several ways, as part of the SCEC broadband validation exercise phase 1 ([Goulet and Abrahamson, 2014](#)). The major revisions include anchoring the HF component to a theoretical level (rather than the LF at the merging frequency) and a different source time function convolved onto the HF scatterograms. BBtoolbox v.1.5 was one of the three methods that passed the SCEC validation exercise, based on comparison of pseudospectral accelerations (PSAs) from synthetic to recorded broadband ground motions for more than 10 historical events ( $M_w$  4.6–7.2) as well as to ground-motion prediction equations (GMPEs;  $M_w$  5.5–6.6 events).

Table 1  
List of Precariously Balanced Rocks (PBRs) Included in Analysis

PBRs		Coordinates in Mesh	$a_1$ (°)	$a_2$ (°)
001-btr	Benton Road	-116.9280129, 33.592667752	11	19
002-gv01	gv01	-117.24549918, 34.277363353	29	36
003-mvt	Mead Valley tipped	-117.25763844, 33.817393437	29	28
004-motte1	motte1_rock	-117.25764160, 33.812388117	8	17
005-gv05	gv05	-117.24852457, 34.279944432	20	20
006-sw01	sw01	-117.34152371, 34.295536945	15	–
007-motte2	Motte2	-117.25765807, 33.80236931	9	24.12
008-spd	South of Perris Dam	-117.18652296, 33.824575788	15	46.1
009-lvm	Lakeview Mountains	-117.07105234, 33.772392190	21.4	44.7
010-pvlm	Pulsar View Lakeview Mountain	-117.08314105, 33.817631772	13	21
011-mvm	Mead Valley mushroom	-117.26375373, 33.822477414	21.88	23.37
012-gpg	Gopher Gulch	-117.36460956, 33.901433630	22.79	24.58
013-lpn	Lake Perris North	-117.16486992, 33.886957443	11	31
014-ucr	UCR	-117.31776094, 33.964182478	25	35
015-sj08	sj08	-116.98565252, 33.895716821	21	21
016-sj06	sj06	-116.98246022, 33.898270027	–	–
017-sj05	sj05	-116.98993160, 33.902274440	12	32
018-sj04	sj04	-116.99280445, 33.904966854	15	26
019-sj02	sj02	-117.00532429, 33.894950876	16	28
020-sj07	sj07	-116.89780871, 33.898982263	32	32

$a_1$ , most likely toppling direction;  $a_2$ , toppling angle when force is applied from a 180° azimuth.

As described above, the LFs are generated by dynamic rupture models, using a CVM with an artificial cutoff of  $V_S^{\min} = 1200$  m/s. However, near-surface  $S$ -wave velocities are typically somewhat lower than this cutoff value at the precarious rock sites; and, for this reason, we apply frequency-dependent amplification functions (Campbell and Bozorgnia, 2008) as a postprocessing step. These amplification functions depend on the ratio between the actual  $V_{S30}$  and that used in the simulations (the reference  $V_S$ ). However, the SCEC CVM- $S$  surface velocities for rock sites tend to be biased high, and the spatial resolution near rock sites surrounded by sediments is limited. For these reasons, we set the  $V_{S30}$  for all PBR sites to be 760 m/s, in agreement with average  $V_{S30}$  values found in connection with PBR site investigations (Pullammanappallil *et al.*, 2006; Louie *et al.*, 2010).

#### PBR Data and Methods

The PBRs considered in this study are indicated by the red triangles in Figure 2. Some of these sites have been used in previous studies to assess shaking intensities of historic and recent paleoseismic earthquakes in inland southern California (Brune, 2002; Brune *et al.*, 2006), as well as in comparison with probabilistic seismic-hazard estimates (Purvance *et al.*, 2008). Many of them, however, have been described more recently, with the specific purpose of assessing ground motions near the Claremont–Casa Loma stepover. Nearly all of the PBRs in this study are the fairly uniform granite of the Perris block, which crops out in low bouldery hills that are characteristic of the region. The exceptions are GV01, GV05, and SW01, which are composed of San Bernardino Mountains granite.

The process of evaluating a PBR for sensitivity to ground motion begins by making a 3D model of the surface of the

rock, from XYZ Cartesian coordinates. For the purpose of this study, this task is accomplished by covering the rock and pedestal with photogrammetric targets, taking photographs from many angles, and processing them into a 3D model with the commercial software Photomodeler.

Photomodeler represents the surface of the rock by connecting the coordinate points of the targets to make abutting scalene triangles. The center of each triangle is considered to be the triangle’s center of mass, and the area of each triangle corresponds to the triangle’s mass relative to the whole rock. The collective center of mass of all the triangles is calculated and plotted in XYZ coordinates then added into the 3D model of the rock. This produced an XYZ coordinate point representing the center of mass of the rock. The azimuth that the rock would most easily topple toward is then determined, and the toppling angle for that azimuth is calculated. Two toppling angles are assigned:  $a_1$  is the direction in which the rock most easily topples and  $a_2$  is the angle in 3D space required to topple the rock when force is applied from an azimuth of 180° from  $a_1$ .

We use this method to model 19 of the 20 PBRs considered in this study; the exception is rock SJ06, which is described by a rougher generic approximation (as a photomodeler representation for this rock is not currently available). Location, size, and shape parameters for each rock are listed in Table 1. We then use the method of Purvance *et al.* (2008) to develop a fragility plot for each rock over a range of peak ground acceleration (PGA) and PGA-normalized spectral accelerations at 1 s (SA-1 s). Figure 5 shows example fragility curves for several of the PBR sites.

To determine PGA and SA-1 s from our model ruptures, we only consider the north–south and east–west components of the synthetic seismograms. We then plot these values for

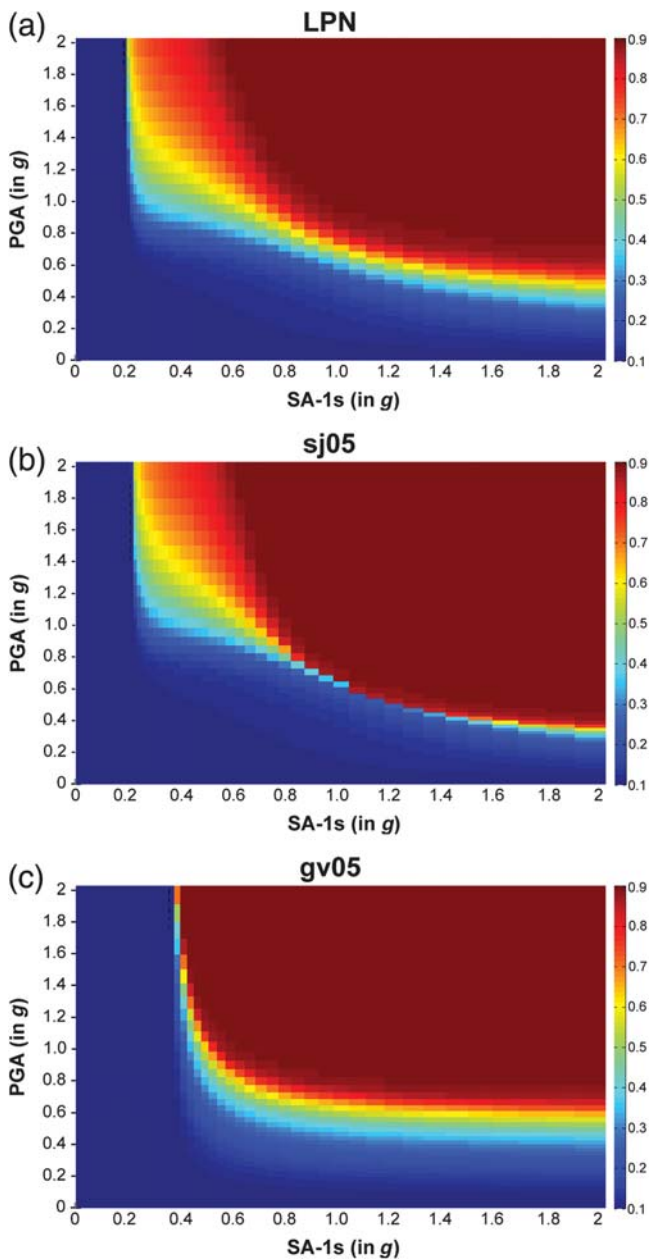


**Figure 5.** Fragility curves for PBR sites (a) LPN, located to the southwest of the SJF; (b) SJ05, located between the SJF and the San Andreas fault; and (c) GV05, located in the San Bernardino Mountains. See Figure 2 for the PBR locations.

each event onto the fragility curve for each rock, to find the toppling probability in that event. Because we are using actual waveforms for these calculations, we do not have to assume that the maximum hazard values for PGA and SA-1 s are generated by the same event; this also allows us to assess which rocks are more sensitive to which of the two parameters. Fragility curves become less precise as probabilities of toppling go to zero; we do not provide exact values for these lowest probabilities due to this loss of precision and describe them as near-zero instead.

## Results

### Dynamic Models

Of the sixteen source models we conducted, only two (scenarios A1 and A2) produce jumping rupture across the stepover, from the Claremont onto the Casa Loma. In both of these cases, the end of the Claremont overlaps a high-stress asperity on the Casa Loma; even then, the rupture does not produce significant slip on the Casa Loma before dying out. The larger of these two scenarios, A1, has a moment magnitude of 6.9. Three of the other model events (B2, C1, and D2) are also  $M_w$  6.9 events, though these ruptures only involve the Claremont strand. Slip distributions for the four largest events are shown in Figure 6. The smallest event modeled is an  $M_w$  5.4; the majority of the model ruptures are in the range of  $M_w$  6.2–6.5 and do not rupture the surface. These magnitudes are consistent with historical events on the SJF; the ones that produce surface rupture at all have an average surface slip of  $\sim 1$  m, as opposed to the average  $\sim 3$  m of surface slip seen in some paleoseismic events (Onderdonk *et al.*, 2015; Rockwell *et al.*, 2015). Slip plots for these models are included in the electronic supplement to this article (Fig. S1). Models with the forced nucleation point on the Casa Loma strand consistently produce shorter ruptures with less slip, and therefore smaller moment, than ruptures with the forced nucleation point on the Claremont strand.

In all cases, rupture remains confined to the high shear stress asperities created by combining the regional and stochastic stress fields, with the largest amounts of slip corresponding to the regions of highest initial shear stress. Because of the pattern of these asperities, the majority of the ruptures do not even approach the stepover region itself and thus do not address the issue of the overall ability of the rupture to jump. However, the Lozos *et al.* (2015) companion study of this stepover, using a larger grid size, included similar models using only the regional stress field. These also did not allow the rupture front to reach the stepover region in most cases, suggesting that features of the fault geometry and assumed regional stress field, independent of any random stress distribution, still discourage jumping rupture.

We chose to take only the four largest dynamic source models (shown in Fig. 6) through to broadband ground-motion modeling. Even though smaller events do not necessarily have weaker shaking than larger ones at high frequencies (affecting PGA), they do at lower frequencies (affecting SA-1 s) that are still critical to toppling PBRs. However, this shaking affects a smaller area. The larger events have the potential to affect more of the PBRs, which makes them better points of comparison against these data. Plots of LF ground motions from the four largest model events are included in Figure S2.

### Broadband Results

Figure 2 shows the location of 20 PBR sites (listed in Table 1) in the vicinity of the three faults involved in the dynamic rupture modeling in our study (Claremont, Farm Road,

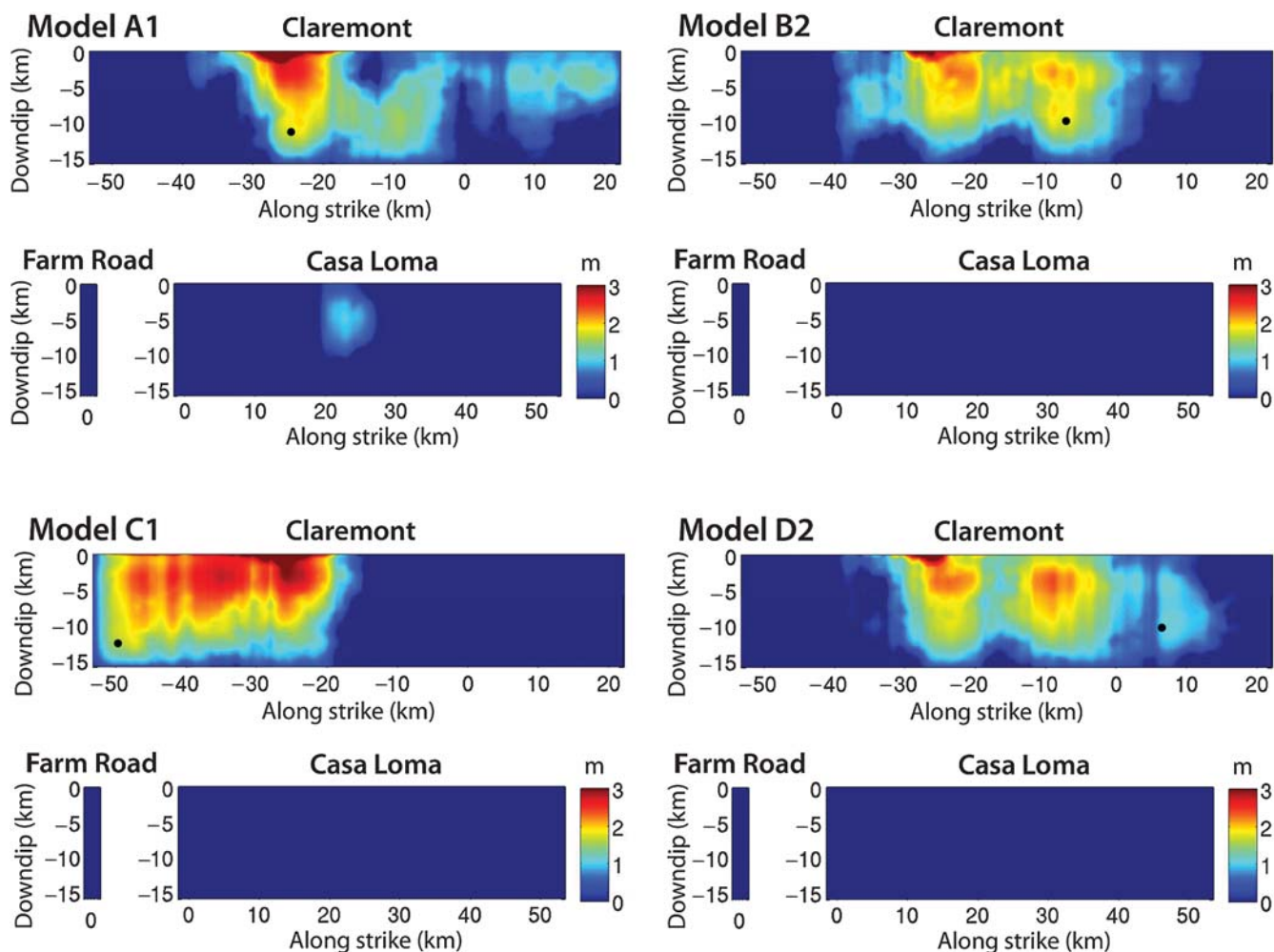


**Figure 6.** Plots of total horizontal slip for the four largest events (each is  $M_w$  6.9) out of the set of 16 total dynamic rupture models. The forced initial nucleation point is indicated by the black dot. These are the models we used to produce the low-frequency ground motions that are used as inputs for the hybrid broadband method.

and Casa Loma). We generated three-component broadband seismograms at all stations for the four selected rupture scenarios, including frequency-dependent site amplification corrections using the method of Olsen and Takedatsu (2014, see ⑤ Figs. S3–S6 for the synthetic accelerograms). The accelerograms are characterized by 10–15 s duration of strong shaking, as expected from an  $M_w \sim 6.9$  event such as the 1989 Loma Prieta, California, earthquake (e.g., Chin and Aki, 1991). To capture the variability from the stochastic component of the scattergrams, we calculated ensemble average PGAs, peak ground velocities (PGVs), and SA-1 s from the synthetic ground motions (Tables 2–4). The largest horizontal PGAs ( $>0.5g$ ) occur at the PBRs SJ05 (0.76g), SJ04 (0.67g), SJ02 (0.57g), LPN (0.57g), and PVLM (0.57g) for scenario C1, and UCR (0.53g) for scenario D2. Horizontal PGVs above 0.4 m/s occur at LPN (0.43 m/s) and SJ06 (0.42 m/s) for scenario B2; at SJ04 (0.45 m/s) and SJ05 (0.41 m/s) for scenario C1; and at UCR (0.40 m/s) for scenario D2. Finally, SA-1 s values exceeding 0.3g are found for at SJ02 (0.30g) for scenario B2, at PVML (0.33g), SJ05

(0.38g), LPN (0.33g), SJ02 (0.34g), SJ04 (0.37g), and SJ05 (0.38g) for scenario C1, and at UCR (0.33g) for scenario D2.

⑤ A comparison between our ensemble PGAs and SA-1 s from our broadband synthetics against leading GMPEs (Abrahamson and Silva, 2008; Boore and Atkinson, 2008; Campbell and Bozorgnia, 2008) using the rotD50 metric (Boore et al., 2006) is shown in Figure S7. In general, the ground-motion intensities from our broadbands fall within one standard deviation of the median values and are therefore considered in agreement with the GMPE predictions. The GMPE values were obtained for  $V_{S30} = 760$  m/s, the values used for the site corrections applied to the broadbands.

It is clear from the broadband ground motions that the cluster of PBRs including SJ02 and SJ04–08 consistently account for some of the largest ground motions due to the close proximity to the Claremont strand ( $\sim 4$  km) and therefore are critical to the toppling analysis. Moreover, rupture directivity is likely an important factor in controlling the peak ground motions, as revealed by the generally larger than median

Table 2  
Horizontal Peak Ground Accelerations ( $g$ ) at the PBRs for the Four Rupture Model Scenarios

Stations	A1		B2		C1		D2	
	North-South	East-West	North-South	East-West	North-South	East-West	North-South	East-West
001-btr	0.10	0.11	0.086	0.097	0.19	0.20	0.11	0.088
002-gv01	0.17	0.14	0.12	0.19	0.099	0.086	0.15	0.16
003-mvt	0.30	0.22	0.19	0.21	0.42	0.39	0.16	0.16
004-motte1	0.13	0.18	0.28	0.34	0.16	0.13	0.27	0.19
005-gv05	0.078	0.086	0.18	0.20	0.13	0.10	0.17	0.24
006-sw01	0.14	0.18	0.10	0.11	0.088	0.059	0.16	0.12
007-motte2	0.30	0.22	0.19	0.20	0.20	0.17	0.20	0.18
008-spd	0.29	0.34	0.42	0.25	0.42	0.45	0.19	0.25
009-lvm	0.20	0.20	0.27	0.18	0.32	0.24	0.13	0.11
010-pvlm	0.23	0.22	0.27	0.33	0.57	0.55	0.17	0.27
011-mvm	0.29	0.20	0.18	0.11	0.20	0.22	0.26	0.19
012-gpg	0.33	0.33	0.20	0.18	0.19	0.16	0.28	0.25
013-lpn	0.27	0.27	0.39	0.37	0.57	0.56	0.27	0.40
014-ucr	0.31	0.26	0.21	0.20	0.21	0.19	0.52	0.53
015-sj08	0.25	0.33	0.32	0.29	0.65	0.41	0.18	0.14
016-sj06	0.25	0.30	0.45	0.35	0.40	0.41	0.28	0.11
017-sj05	0.16	0.15	0.33	0.26	0.76	0.67	0.39	0.47
018-sj04	0.30	0.28	0.23	0.35	0.34	0.66	0.34	0.22
019-sj02	0.18	0.25	0.24	0.24	0.57	0.44	0.28	0.20
020-sj07	0.16	0.19	0.20	0.18	0.40	0.33	0.20	0.15

GMPE values of PGA, PGV, and SA-1 s toward the south-eastern end of the Claremont strand in scenario C1 (e.g., SJ02 and SJ04-8), in which rupture nucleated at the northwestern end of the Claremont and propagated southeastward. On the other hand, peak motions at SW01, GV01, and GV05, located near the initiation of rupture and mostly in the backward rupture direction for scenario C1, experienced lower than the median GMPE ground-motion intensities.

### PBR Results

Essentially all of the waveforms at all of the PBR sites have a near-zero or very low probability of toppling the rocks. Nonzero probabilities are found at site SJ06 (5%) for scenario A1 and at SJ08 and SJ05 (5%) for scenario C1. However, because our fragility calculations are based on extrapolations from synthetic seismograms rather than from PSHAs, any toppling probability of 20% or lower is questionably different from zero. Thus, the distribution of precarious rocks is consistent with the ground motions from these model earthquakes.

### Discussion

The complexity of our SJF parameterization is such that our models produce events of a size consistent with historic  $M_w \sim 6-7$  SJF earthquakes but smaller than typical  $M_w \sim 7-7.5$  paleoseismic events. As mentioned above, and described at length in the companion article to this study (Lozos *et al.*, 2015), rupture propagation remains confined to high-stress asperities, because the energy budget of the rupture becomes so skewed toward fracture when it reaches the edge of the asperity that it is not able to propagate far into the

unfavorable portions of the fault. The shape of these asperities in our models is defined by the combination of the regional stress field with stochastic stresses. Because the prestress field in our models is a combination of several types of complexity, however, it is difficult to say which factor may be dominant on the real-world SJF. Although our choice of length scale for the stochastic asperities produces event sizes that match the historical record, the models of Lozos *et al.* (2014) suggest that geometry alone can also constrain model ruptures to be consistent with historical earthquakes. Had we implemented larger stochastic asperities, our models would have produced ruptures more comparable to paleoseismic-type events.

Part of our motivation for including stochastic stresses in these models was to account for stress concentrations that arise from fault interactions. As such, an asperity of the size needed to produce a rupture that is consistent with the large paleoseismic-type events may develop as a result of accumulated stress changes from a number of historically sized earthquakes on the SJF or other nearby faults. Any rupture barrier, whether geometrical or otherwise, will eventually be brought to its failing point, as it has to release the stresses it accumulates from ruptures stopping there. Thus, we suggest the large paleoseismic-type ruptures may nucleate in geometrically unfavorable locations that do not slip in small historic-type events. Stress conditions that allow rupture propagation through these barriers will also promote energetic propagation through sections of the fault that are consistently more favorable for rupture, even if they have released stress in more recent small events.

The result that the Claremont strand consistently has larger events than the Casa Loma strand is a combined effect of geometry and stress orientation. The Claremont strand is

Table 3  
Horizontal SA-1 s (g) Values at the PBRs for the Four Rupture Model Scenarios

Stations	A1		B2		C1		D2	
	North–South	East–West	North–South	East–West	North–South	East–West	North–South	East–West
001-btr	0.061	0.078	0.055	0.050	0.092	0.101	0.049	0.046
002-gv01	0.077	0.066	0.085	0.10	0.19	0.15	0.12	0.11
003-mvt	0.14	0.083	0.10	0.089	0.18	0.20	0.091	0.094
004-motte1	0.077	0.094	0.17	0.15	0.096	0.081	0.096	0.098
005-gv05	0.051	0.046	0.087	0.083	0.20	0.16	0.15	0.13
006-sw01	0.078	0.076	0.067	0.096	0.13	0.048	0.12	0.13
007-motte2	0.15	0.085	0.12	0.079	0.14	0.10	0.097	0.077
008-spd	0.14	0.17	0.18	0.091	0.21	0.24	0.085	0.086
009-lvm	0.12	0.12	0.12	0.081	0.26	0.13	0.11	0.072
010-pvlm	0.11	0.14	0.14	0.17	0.25	0.33	0.13	0.14
011-mvm	0.11	0.10	0.11	0.052	0.13	0.13	0.12	0.080
012-gpg	0.15	0.14	0.14	0.12	0.25	0.19	0.27	0.22
013-lpn	0.12	0.15	0.21	0.20	0.33	0.31	0.15	0.19
014-ucr	0.15	0.14	0.18	0.12	0.24	0.24	0.28	0.33
015-sj08	0.26	0.19	0.25	0.18	0.28	0.28	0.17	0.099
016-sj06	0.24	0.22	0.29	0.15	0.16	0.25	0.19	0.090
017-sj05	0.18	0.16	0.26	0.19	0.36	0.38	0.22	0.19
018-sj04	0.21	0.20	0.24	0.20	0.19	0.37	0.22	0.16
019-sj02	0.21	0.23	0.30	0.20	0.29	0.34	0.27	0.17
020-sj07	0.22	0.19	0.22	0.14	0.21	0.21	0.17	0.10

SA-1 s, peak spectral acceleration at 1 s.

more planar than the Casa Loma in this interpretation of the fault geometry. It is also more favorably aligned within the current regional stress field (see the companion article [Lozos *et al.*, 2015] for more discussion of this effect). However, as mentioned previously, the paleoseismic record for both strands includes events with an average of  $\sim 3$  m of surface slip and does not capture smaller ruptures that do not reach the surface. A smoother fault geometry at depth would likely also permit longer ruptures on both strands. Resolving the regional stress field onto a smoother fault trace would produce larger concentrations of both high and low stress, and in a way that is more physically determined than an arbitrary choice of stochastic stress length scale. However, given that these large paleoseismic-type events are not as common as smaller historic-type events, this still implies that stress changes induced by factors other than the geometry of the SJF alone are needed to promote an end-to-end rupture on the Casa Loma–Clark strand.

In addition to localized stress change patterns associated with rupture on a single fault, rotations of regional stresses have been observed and documented after large earthquakes in southern California (Hauksson, 1994; Hardebeck and Hauksson, 2001). Rotations of  $10^\circ$  in either direction from N7°E produced very different rupture patterns on this same fault geometry in lower-resolution models (Lozos *et al.*, 2015). It is possible that the average stress field at the time of the last large Casa Loma–Clark event was oriented differently from the current regional stress orientation of N7°E. This rotation, along with the accumulation of stress at barriers described above, is a multicycle effect, which therefore would not arise in single-event models such as the ones presented here. It is another possible explanation as to why our models do not produce rup-

tures that match the paleoseismic-type events. Multicycle modeling of the SJF and nearby faults will be useful to address this bimodal-event-size behavior.

Our model event sizes, as well as the historic and paleoseismic record of SJF earthquakes, are at odds with the most recent Uniform California Earthquake Rupture Forecast (UCERF3, Field *et al.*, 2013). UCERF3 suggests that the SJF has an  $M_w$  7.4–8.3 rupture, on average, every 200 yrs and few events below  $M_w$  7. However, the historic record alone shows that  $M_w < 7$  events are a common and frequent SJF behavior, even without analysis of the physical processes that produce this event size. As discussed above, our models produce events comparable to historic ruptures due in part to complex fault geometry. In contrast, UCERF3 parameterizes the entire SJF as a single continuous fault, omitting the primary rupture barrier of the stepover. The complexity of our models may keep ruptures too short, but the simplicity of the UCERF3 geometry may allow ruptures to become too long. The lower estimate of UCERF3’s maximum San Jacinto event size,  $M_w$  7.4, is consistent with paleoseismic-type events. However, magnitude-scaling calculations (Wells and Coppersmith, 1994) indicate that an  $M_w$  8.3 rupture consistent with the paleoseismic average  $\sim 3$  m slip per event would require a length of over 1000 km, given a common seismogenic depth of 16 km between our models and UCERF3. This is substantially longer than the entire SJF. Although some paleoseismic ages correlate between the Claremont and the Casa Loma–Clark, there is no such correlation with the Coyote Creek strand to the south (Rockwell *et al.*, 2015). A higher stress drop would somewhat decrease this required length; however, as our LF dynamic models of this stepover (Lozos *et al.*, 2015) show,

Table 4  
Horizontal Peak Ground Velocities (m/s) at the PBRs for the Four Rupture Model Scenarios

Stations	A1		B2		C1		D2	
	North–South	East–West	North–South	East–West	North–South	East–West	North–South	East–West
001-btr	0.060	0.085	0.072	0.064	0.10	0.13	0.053	0.056
002-gv01	0.10	0.10	0.10	0.12	0.18	0.14	0.15	0.12
003-mvt	0.19	0.15	0.15	0.090	0.22	0.24	0.14	0.091
004-motte1	0.12	0.14	0.21	0.17	0.15	0.11	0.15	0.11
005-gv05	0.085	0.078	0.12	0.12	0.18	0.14	0.17	0.15
006-sw01	0.11	0.11	0.088	0.10	0.20	0.13	0.18	0.17
007-motte2	0.17	0.15	0.16	0.11	0.16	0.12	0.14	0.093
008-spd	0.19	0.22	0.24	0.16	0.25	0.27	0.12	0.14
009-lvm	0.13	0.15	0.23	0.15	0.17	0.20	0.18	0.070
010-pvlm	0.13	0.18	0.26	0.30	0.30	0.34	0.13	0.20
011-mvm	0.19	0.16	0.16	0.064	0.18	0.14	0.15	0.095
012-gpg	0.20	0.21	0.22	0.15	0.30	0.16	0.28	0.20
013-lpn	0.20	0.27	0.43	0.21	0.32	0.37	0.26	0.25
014-ucr	0.30	0.17	0.27	0.15	0.36	0.23	0.37	0.40
015-sj08	0.30	0.24	0.32	0.37	0.28	0.33	0.32	0.11
016-sj06	0.27	0.22	0.42	0.30	0.24	0.34	0.32	0.11
017-sj05	0.25	0.20	0.36	0.34	0.38	0.41	0.34	0.27
018-sj04	0.27	0.26	0.29	0.35	0.23	0.45	0.33	0.19
019-sj02	0.25	0.23	0.35	0.43	0.33	0.36	0.37	0.18
020-sj07	0.27	0.17	0.27	0.31	0.28	0.30	0.33	0.15

a higher stress drop produces larger slip and stronger ground motions. These stronger motions, as well as the higher SA-1  $s$  that would be produced by an  $M_w$  8.3 rupture, would likely increase toppling probabilities for the PBRs.

The velocity structure proves to have the most controlling influence on the ground motion. Our lower-resolution dynamic models (Lozos *et al.*, 2015) produce their strongest ground motions in sedimentary basins, most notably the San Bernardino basin and, to a lesser degree, the San Jacinto Valley. Outside of the basins, the strongest shaking is confined within  $\sim 5$  km of the fault. The lineament of precarious rocks between the San Jacinto and Elsinore faults, as described by Brune *et al.* (2006), is consistent with these results, as the majority of these rocks are over 10 km from either fault.

Rupture directivity has little effect on LF ground motion within a narrow basin that is directly on the fault; however, ground-motion distributions and intensities from parts of the fault that cut through harder rock are more affected by directivity and by velocity structure in the far field (Lozos *et al.*, 2015). In our LF models, northward-directed rupture on the Claremont strand, for example, is more likely to excite stronger ground motions toward the northwest, specifically in the San Bernardino Valley and Cajon Pass, whereas southward-directed rupture on the Claremont produces stronger shaking in the San Jacinto Valley and San Gorgonio Pass, even if rupture does not jump.

PBRs do not occur on sedimentary basins, as these formations cannot weather out of solid bedrock that is covered with several kilometers of sediment (Bell *et al.*, 1998). All of the PBRs in this study are on solid rock sites; the amplified ground motions in the basins within our model do not significantly affect the PBRs. All experience a near-zero prob-

ability of being toppled in any of our model events, despite many of them being within 5 km of the fault. Thus, the existence and position of these rocks is consistent with all of our models. This means we are not able to use the precarious rocks to rule out any of our model scenarios. However, this also implies that even the largest events in the 2000–4000 yr paleoseismic record have not produced ground motions strong enough to topple these near-fault PBRs over the time that the rocks have been precarious. The fact that the majority of the PBRs, including the cluster of sites SJ02 and SJ04–SJ08, are toward the southeastern end of the Claremont strand, very close to the stepover, while relatively few exist in Cajon Pass and the San Bernardino Mountains, may imply a preferential northward rupture direction on the Claremont strand.

We are not able to elaborate on whether the persistence of the rocks closest to the stepover region is a result of weaker shaking between the faults within a single event. This is largely because neither of our models that produced jumping rupture involved sustained rupture on both the Claremont and Casa Loma–Clark strands and because we only calculated broadband ground motions for one of these two. However, the paleoseismology of the Claremont and Casa Loma–Clark strands includes several events on both strands that overlap in time, which could be interpreted as single ruptures that jumped the stepover (Rockwell *et al.*, 2015). If these did occur, they did not produce ground motions strong enough to topple the rocks. This is consistent with the idea of reduced ground motion within the stepover, though the gap in strong motion would only coincide with the position of the SJ02/SJ04–SJ08 cluster of PBRs if the rupture began on the Casa Loma–Clark and propagated northward onto the Claremont (Brune, 2003; Lozos *et al.*, 2013).

Our models produce ground motions that are a good match to several of the empirical GMPEs (Abrahamson and Silva, 2008; Boore and Atkinson, 2008; Campbell and Bozorgnia, 2008) used in producing the National Seismic Hazard Map (Petersen *et al.*, 2014). This good match between real and synthetic ground motions suggests that a hybrid modeling method such as the one used here may be useful to produce realistic near-field records for large events, which could be used to fill in the gap in that magnitude and distance range for future GMPE refinement. These types of models and comparisons with fragile geological structures may also be useful for localized refinement of seismic-hazard maps.

The precarious rocks and the model ruptures alike emphasize that the Claremont/Casa Loma–Clark stepover is a robust barrier to rupture and that only rare events may slip both strands at once. Complexity of the fault trace, the stress field, and the velocity structure combine to result in short ruptures with subshear rupture velocity and a limited area of strong shaking, even with initial stress drop and fault strength values that would result in prolonged supershear rupture on a planar fault in a homogeneous setting. Because the asperities in our models were generated randomly, we cannot say that our models produced events that are completely analogous to past events or possible future ones. A better understanding of the location of the real asperities would be necessary to assess this. However, the general consistency of our models with the historic behavior of the San Jacinto implies that a great deal of heterogeneity is controlling that behavior. The precarious rock data emphasizes that our modeled ground motions, despite the random asperities, are consistent with empirical GMPEs for this region.

### Conclusions

The historic rupture behavior of the SJF is characterized by moderate events constrained to a single strand of the fault. Our dynamic model results are consistent with this behavior and imply that on-fault stress heterogeneity that arises from geometrical complexity, nearby earthquakes, and long-term fault interactions is what keeps these historic-type ruptures confined to relatively short lengths. Under the current regional stress orientation, the Claremont strand is more favorable for longer ruptures than is the Casa Loma–Clark strand. Paleoseismic records include larger events on the northern San Jacinto, possibly involving both strands; this observation suggests the stress conditions required to produce larger events evolve over multiple smaller earthquake cycles. Future modeling studies accounting for this evolution of stresses will be needed to assess what conditions are necessary to produce these longer ruptures.

All of our simulated broadband ground motions are consistent with the distribution of PBRs near the SJF; none of the rocks experience a toppling probability of significantly greater than zero in any of our scenario earthquakes. The PBRs do not allow us to rule out any of our scenarios, but they do emphasize that our model rupture behaviors are consistent with real behaviors.

The presence of PBRs also suggests that, even in the larger events that are inferred from paleoseismic data but do not occur in our models, strong ground motions are confined to basin areas and immediately adjacent to the fault (less than  $\sim 3$  km). It is interesting to note both that the greatest concentration of PBRs in the model area is close to the stepover region and that the majority of the PBRs that experience nonzero toppling probabilities are within this cluster. The peak motions responsible for these nonzero (although consistent with the presence of the PBRs) toppling probabilities in our models are typically affected by rupture directivity effects (e.g., the large peak motions at the SJ PBR cluster for scenario C1 initiating at the northwest end of the Claremont strand). It is a reasonable assumption that this rupture configuration would be most likely to generate toppling probabilities in the range inconsistent with the PBRs for the rare, large events not captured by our limited sample of rupture models. Moreover, there are relatively few mapped PBRs to the northwestern end of the Claremont and southeastern end of the Casa Loma–Clark. These findings may imply preferred rupture directions of southeast to northwest on the Claremont strand and, to a lesser degree, northwest to southeast on the Casa Loma–Clark, in both cases away from the stepover.

Our ground-motion results match intensities calculated by empirical GMPEs (Abrahamson and Silva, 2008; Boore and Atkinson, 2008; Campbell and Bozorgnia, 2008). This good correlation between models and observations suggests that models may be useful for filling in gaps in the observational record used for GMPE development. Using realistic synthetic ground motions in future GMPEs may help reduce the apparent discrepancy between the highest predicted ground motions in the National Seismic Hazard Map (Petersen *et al.*, 2014) and the values needed to topple the PBRs.

Our model rupture lengths are shorter than the largest events found in the paleoseismic record (Onderdonk *et al.*, 2015; Rockwell *et al.*, 2015), though both are inconsistent with the maximum SJF event sizes predicted by UCERF3 (Field *et al.*, 2013). A rupture energetic enough to match the UCERF3 maximum event size would produce more slip than in our models or in the paleoseismic record and may result in ground motions strong enough to topple many of the PBRs in our study area. Our results therefore suggest that UCERF's maximum event sizes for the SJF are implausible. We suggest that realistically complex dynamic rupture simulations may help constrain plausible behaviors for major faults in future probabilistic earthquake rupture forecasts and that hybrid deterministic-stochastic broadband ground-motion modeling of regions and faults currently identified as high hazard may help refine and constrain values for future seismic-hazard mapping.

### Data and Resources

Some of the precariously balanced rock sites considered in this study are discussed in previous studies (Brune, 1996, 2002; Brune *et al.*, 2006; Purvance *et al.*, 2008), though not

in the context of dynamic rupture simulations. All of our results were generated using FaultMod (Barall, 2009) or BBToolbox v.1.5 (Olsen and Takedatsu, 2014). Our model's fault geometry along strike is based on the U.S. Geological Survey (USGS) *Quaternary Fault and Fold Database for the United States* (2010), available at <http://earthquake.usgs.gov/hazards/qfaults/> (last accessed October 2014). A modified version of Figure 1 also appears in the companion, Lozos *et al.* (2015). All other figures were generated specifically for this article.

### Acknowledgments

The authors would like to thank Glenn Biasi, James Dieterich, Gareth Funning, and Annemarie Baltay for helpful conversation and commentary about this work. We would also like to thank Michel Bouchon and one anonymous reviewer. Funding for this research was provided by U.S. Geological Survey (USGS) National Earthquake Hazards Reduction Program (NEHRP) Grants G12AP20064 and G12AP2006, as well as by National Science Foundation Awards EAR-1349180, EAR-1226343, and OCI-1148493. Julian Lozos is supported by a National Science Foundation Earth Science Postdoctoral Fellowship under Award EAR-PF-1250143.

### References

- Abrahamson, N. A., and W. J. Silva (2008). Summary of the Abrahamson & Silva NGA ground-motion relations, *Earthq. Spectra* **24**, no. 1, 67–97.
- Allen, C. R., A. Grantz, J. N. Brune, M. M. Clark, R. V. Sharp, T. G. Theodore, E. W. Wolfe, and M. Wyss (1968). The Borrego Mountain, California, earthquake of 9 April 1968: A preliminary report, *Bull. Seismol. Soc. Am.* **58**, 1183–1186.
- Andrews, D. J. (1976). Rupture propagation with finite stress in antiplane strain, *J. Geophys. Res.* **81**, 3575–3582.
- Andrews, D. J., and M. Barall (2011). Specifying initial stress for dynamic heterogeneous earthquake source models, *Bull. Seismol. Soc. Am.* **101**, 2408–2417.
- Andrews, D. J., and Y. Ben-Zion (1997). Wrinkle-like slip pulse on a fault between different materials, *J. Geophys. Res.* **102**, 553–571.
- Aochi, H., E. Fukuyama, and M. Matsu'ura (2000). Spontaneous rupture propagation on a non-planar fault in 3-D elastic medium, *Pure Appl. Geophys.* **157**, 2003–2027.
- Barall, M. (2009). A grid-doubling technique for calculating dynamic three-dimensional spontaneous rupture on an earthquake fault, *Geophys. J. Int.* **178**, 845–859.
- Bell, J. W., J. N. Brune, T. Liu, M. Zerda, and J. C. Yount (1998). Dating the precariously balanced rocks in seismically active parts of California and Nevada, *Geology* **26**, 495–498.
- Blisniuk, K., T. Rockwell, L. Owen, M. Oskin, C. Lippincott, M. Caffee, and J. Dortch (2010). Late Quaternary slip rate gradient defined using high-resolution topography and <sup>10</sup>Be dating of offset landforms on the southern San Jacinto fault zone, California, *J. Geophys. Res.* **115**, no. B08401, 1–11.
- Boore, D. M., and G. M. Atkinson (2008). Ground-motion prediction equations for the average horizontal component of PGA, PGV, and 5%-damped PSA at spectral periods between 0.01 and 10.0 s, *Earthq. Spectra* **24**, no. 1, 99–138.
- Boore, D. M., J. Watson-Lamprey, and N. A. Abrahamson (2006). Orientation-independent measures of ground motion, *Bull. Seismol. Soc. Am.* **96**, 1502–1511.
- Brune, J. N. (1996). Precariously balanced rocks and ground motion maps for southern California, *Bull. Seismol. Soc. Am.* **86**, 43–54.
- Brune, J. N. (2002). Precariously-rock constraints on ground motion from historic and recent earthquakes in southern California, *Bull. Seismol. Soc. Am.* **92**, 2602–2611.
- Brune, J. N. (2003). Precarious rock evidence for low near-source accelerations for trans-tensional strike-slip earthquakes, *Phys. Earth Planet. In.* **137**, doi: [10.1016/S0031-9201\(03\)00017-7](https://doi.org/10.1016/S0031-9201(03)00017-7).
- Brune, J. N., A. Anooshehpour, M. D. Purvance, and R. J. Brune (2006). Band of precariously balanced rocks between the Elsinore and San Jacinto, California, fault zones: Constraints on ground motion for large earthquakes, *Geology* **34**, 137–140.
- Campbell, K. W., and Y. Bozorgnia (2008). NGA ground motion model for the geometric mean horizontal component of PGA, PGV, PGD and 5% damped linear elastic response spectra for periods ranging from 0.01 to 10 s, *Earthq. Spectra* **24**, no. 1, 139–171.
- Chin, B.-H., and K. Aki (1991). Simultaneous study of the source, path, and site effects on strong motion during the 1989 Loma Prieta earthquake: A preliminary on pervasive nonlinear site effects, *Bull. Seismol. Soc. Am.* **81**, 1859–1884.
- Duan, B., and D. D. Oglesby (2007). Nonuniform prestress from prior earthquakes and the effect on dynamics on branched fault systems, *J. Geophys. Res.* **112**, no. B05308, doi: [10.1029/2006JB004443](https://doi.org/10.1029/2006JB004443).
- Fialko, Y. (2006). Interseismic strain accumulation and the earthquake potential of the southern San Andreas fault system, *Nature* **441**, 968–971.
- Field, E. H., G. P. Biasi, P. Bird, T. E. Dawson, K. R. Felzer, D. D. Jackson, K. M. Johnson, T. H. Jordan, C. Madden, A. J. Michael, *et al.* (2013). Uniform California earthquake rupture forecast, version 3 (UCERF3)—The time-independent model, *U.S. Geol. Surv. Open-File Rept. 2013-116*, California Geological Survey Special Report 228, and Southern California Earthquake Center Publication 1792.
- Goulet, C. A., and N. A. Abrahamson (2014). The SCEC broadband platform validation exercise: Methodology for code validation in the context of seismic hazard analyses, *Seismol. Res. Lett.* **86**, no. 1, doi: [10.1785/0220140104](https://doi.org/10.1785/0220140104).
- Hardebeck, J. L., and E. Hauksson (2001). Crustal stress field in southern California and its implications for fault mechanics, *J. Geophys. Res.* **106**, 21,859–21,882.
- Harris, R. A., and S. M. Day (1993). Dynamics of fault interaction: Parallel strike-slip faults, *J. Geophys. Res.* **98**, 4461–4472.
- Harris, R. A., and S. M. Day (1997). Effects of a low-velocity zone on dynamic rupture, *Bull. Seismol. Soc. Am.* **87**, 1267–1280.
- Harris, R. A., M. Barall, R. Archuleta, E. Dunham, B. Aagaard, J. P. Ampuero, H. Bhat, V. Cruz-Atienza, L. Dalguer, P. Dawson, *et al.* (2009). The SCEC/USGS dynamic earthquake rupture code validation exercise, *Seismol. Res. Lett.* **80**, 119–126, doi: [10.1785/gssrl.80.1.119](https://doi.org/10.1785/gssrl.80.1.119).
- Hauksson, E. (1994). State of stress from focal mechanisms before and after the 1992 Landers earthquake sequence, *Bull. Seismol. Soc. Am.* **84**, 917–934.
- Hole, J. A. (1992). Non-linear high resolution three-dimensional seismic travel time tomography, *J. Geophys. Res.* **97**, 6553–6562.
- Ida, Y. (1972). Cohesive force across the tip of a longitudinal shear crack and Griffith's specific surface energy, *J. Geophys. Res.* **77**, 3796–3805.
- Kame, N., J. R. Rice, and R. Dmowska (2003). Effects of pre-stress state and rupture velocity on dynamic fault branching, *J. Geophys. Res.* **108**, 2265, doi: [10.1029/2002JB002189](https://doi.org/10.1029/2002JB002189).
- Kendrick, K. J., and D. M. Morton (2012). Geomorphic evidence for structural evolution of the northern San Jacinto fault zone in the San Timoteo badlands, *Seismological Society of America Annual Meeting*, San Diego, California, 17–19 April 2012, Conference Presentation.
- Lin, G., P. M. Shearer, and E. Hauksson (2007). Applying a three-dimensional velocity model, waveform cross correlation, and cluster analysis to locate southern California seismicity from 1981 to 2005, *J. Geophys. Res.* **112**, doi: [10.1029/2007JB004986](https://doi.org/10.1029/2007JB004986).
- Louie, J. N., J. N. Brune, and S. K. Pullammanappallil (2010). Estimates of  $V_{S100}$  at sites of precariously balanced rocks, *2010 SCEC Annual Meeting*, September 2010 poster 1-073, <http://www.scec.org/meetings/2010am/index.html> (last accessed August 2014).
- Lozos, J. C., D. D. Oglesby, and J. N. Brune (2013). The effects of fault stopovers on ground motion, *Bull. Seismol. Soc. Am.* **103**, 1922–1934.
- Lozos, J. C., D. D. Oglesby, J. N. Brune, and K. B. Olsen (2012). Small intermediate fault segments can either aid or hinder rupture propagation

- at stepovers, *Geophys. Res. Lett.* **39**, L18305, doi: [10.1029/2012GL053005](https://doi.org/10.1029/2012GL053005).
- Lozos, J. C., D. D. Oglesby, J. N. Brune, and K. B. Olsen (2015). Rupture and ground motion models on the northern San Jacinto fault, incorporating realistic complexity, *Bull. Seismol. Soc. Am.* **105**, no. 4, doi: [10.1785/0120140327](https://doi.org/10.1785/0120140327).
- Lozos, J. C., T. K. Rockwell, and N. W. Onderdonk (2014). Dynamic rupture models of the historic and recent paleoseismic rupture sequence of the northern and central San Jacinto fault, *SCEC Proceedings and Abstracts*, Anchorage, Alaska, 30 April–2 May 2014, Vol. 24, 119.
- Magistrale, H., S. Day, R. Clayton, and R. Graves (2000). The SCEC southern California reference three-dimensional seismic velocity model version 2, *Bull. Seismol. Soc. Am.* **90**, no. 6B, S65–S76.
- Mai, P. M., and G. C. Beroza (2003). A hybrid method for calculating near-source, broadband seismograms: Application to strong motion prediction, *Phys. Earth Planet. In.* **137**, no. 1/4, 183–199.
- Mai, P. M., W. Imperatori, and K. B. Olsen (2010). Hybrid broadband ground-motion simulations: Combining long-period deterministic synthetics with high-frequency multiple *S*-to-*S* backscattering, *Bull. Seismol. Soc. Am.* **100**, no. 5A, 2124–2142, doi: [10.1785/0120080194](https://doi.org/10.1785/0120080194).
- Mena, B., P. M. Mai, K. B. Olsen, M. D. Purvance, and J. N. Brune (2010). Hybrid broadband ground-motion simulation using scattering Green's functions: Application to large-magnitude events, *Bull. Seismol. Soc. Am.* **100**, no. 5A, 213–2122, doi: [10.1785/0120080318](https://doi.org/10.1785/0120080318).
- Oglesby, D. D. (2008). Rupture termination and jump on parallel offset faults, *Bull. Seismol. Soc. Am.* **98**, 440–447.
- Olsen, K. B., and R. Takedatsu (2014). The SDSU broadband ground motion generation module BBtoolbox version 1.5, *Seismol. Res. Lett.* **86**, no. 1, doi: [10.1785/0220140102](https://doi.org/10.1785/0220140102).
- Onderdonk, N. W., S. F. McGill, and T. K. Rockwell (2015). Short-term variations in slip rate and size of pre-historic earthquakes during the past 2000 years on the northern San Jacinto fault zone, a major plate boundary in southern California, *Lithosphere* **7**, doi: [10.1130/L393.1](https://doi.org/10.1130/L393.1).
- Onderdonk, N. W., T. K. Rockwell, S. F. McGill, and G. I. Marliyani (2013). Evidence for seven surface ruptures in the past 1600 years on the Claremont fault at Mystic Lake, northern San Jacinto fault zone, California, *Bull. Seismol. Soc. Am.* **103**, 519–541.
- Palmer, A. C., and J. R. Rice (1973). The growth of slip surfaces in the progressive failure of overconsolidated clay, *Proc. Math. Phys. Sci.* **332**, 527–548.
- Park, S. K., D. Pendergraft, W. J. Stephenson, K. M. Shedlock, and T. C. Lee (1995). Delineation of intrabasin structure in a dilational jog of the San Jacinto fault zone, southern California, *J. Geophys. Res.* **100**, 691–702.
- Petersen, M. D., M. P. Moschetti, P. M. Powers, C. S. Mueller, K. M. Haller, A. D. Frankel, Y. Zeng, S. Rezaeian, S. C. Harmsen, O. S. Boyd, *et al.* (2014). Documentation for the 2014 update of the United States National Seismic Hazard Maps, *U.S. Geol. Surv. Open-File Rept.* 2014–1091.
- Plesch, A., J. H. Shaw, C. Benson, W. A. Bryant, S. Carena, M. Cooke, J. Dolan, G. Fuis, E. Gath, L. Grant, *et al.* (2007). Community fault model (CFM) for southern California, *Bull. Seismol. Soc. Am.* **97**, 1793–1802.
- Pullammanappallil, S. K., M. D. Purvance, and J. N. Brune (2006). Refraction microtremor (ReMi) results for  $V_{530}$  at precarious rock sites between the Elsinore and San Jacinto faults, 2006 SCEC Annual Meeting, poster abstract, <http://www.scec.org/meetings/2006am/index.html> (last accessed August 2014).
- Purvance, M., J. Brune, N. A. Abrahamson, and J. G. Anderson (2008). Consistency of precariously balanced rocks with probabilistic seismic hazard estimates in southern California, *Bull. Seismol. Soc. Am.* **98**, 2629–2640, doi: [10.1785/0120080169](https://doi.org/10.1785/0120080169).
- Rockwell, T. K., T. Dawson, J. Young, and G. G. Seitz (2015). A 21-event, 4000-year history of surface ruptures in the Anza seismic gap, San Jacinto fault: Implications for long-term earthquake production on a major plate boundary fault, *Pure Appl. Geophys.* **171**, 2955–2965.
- Salisbury, J. B., T. K. Rockwell, T. J. Middleton, and K. W. Hudnut (2012). LiDAR and field observations of slip distribution for the most recent surface ruptures along the central San Jacinto fault, *Bull. Seismol. Soc. Am.* **102**, 598–619.
- Sanders, C. O., and H. Kanamori (1984). A seismotectonic analysis of the Anza seismic gap, San Jacinto fault zone, southern California, *J. Geophys. Res.* **89**, 5873–5890.
- Topozada, T., D. Branum, M. Reichle, and C. Hallstrom (2002). San Andreas fault zone, California:  $M \geq 5.5$  earthquake history, *Bull. Seismol. Soc. Am.* **92**, 2555–2601.
- Wells, D. L., and K. J. Coppersmith (1994). New empirical relationships among magnitude, rupture length, rupture width, rupture area, and surface displacement, *Bull. Seismol. Soc. Am.* **84**, 974–1002.
- Wesnousky, S. G. (2008). Displacement and geometrical characteristics of earthquake surface ruptures: Issues and implications for seismic-hazard analysis and the process of earthquake rupture, *Bull. Seismol. Soc. Am.* **98**, 1609–1632.
- Zeng, Y., F. Su, and K. Aki (1991). Scattering wave energy propagation in a random isotropic scattering medium 1. Theory, *J. Geophys. Res.* **96**, no. B1, 607–619.
- Zeng, Y. H., K. Aki, and T. L. Teng (1993). Mapping of the high-frequency source radiation for the Loma Prieta earthquake, California, *J. Geophys. Res.* **98**, no. B7, 11,981–11,993.

Department of Earth Sciences  
University of California, Riverside  
Riverside, California 92521  
david.oglesby@ucr.edu  
(J.C.L., D.D.O.)

Department of Geological Sciences  
San Diego State University  
MC-1020  
5500 Campanile Drive  
San Diego, California 92182-1020  
kbolsen@mail.sdsu.edu  
rtakedatsu@mail.sdsu.edu  
(K.B.O., R.T.)

Department of Geological Sciences  
University of Nevada, Reno  
1664 North Virginia Street  
Reno, Nevada 89557-0172  
brune@seismo.unr.edu  
richbrune@sbcglobal.net  
(J.N.B., R.J.B.)

Manuscript received 30 October 2014;  
Published Online 7 July 2015